nature communications

Article

https://doi.org/10.1038/s41467-025-63095-w

Optical focusing into scattering media via iterative time reversal guided by absorption nonlinearity

Received: 25 September 2024

Accepted: 6 August 2025

Published online: 21 August 2025

Check for updates

Manxiu Cui, S. Süleyman Kahraman & Lihong V. Wang

Guide star-assisted time-reversal enables deep optical focusing in scattering media such as biological tissue, overcoming the diffusion limit of light. However, in practice, guide stars formed using contrast agents or ultrasonic modulation naturally occupy regions much larger than the optical resolution, thus limiting their effectiveness. We propose and experimentally demonstrate a time-reversal focusing mechanism in scattering media that achieves focusing to a single speckle grain without the need for point-like guide stars. We exploit optical absorption nonlinearity as a light-induced perturbation to create virtual guide stars. The back-scattered fields in response to high- and low-intensity illuminations are subtracted after scaling to synthesize the field from the dominant speckle grains in the medium. We use this time-reversed field as the incident illumination in subsequent iterations. The focusing is achieved despite the extended layer of nonlinear absorber via a positive feedback loop that favors higher-intensity speckle grains, converging to a single virtual guide star at the optical resolution. We also demonstrate that by adding a phase ramp in each iteration, this focus can be gradually steered beyond the memory effect range.

The scattering of light in complex media renders most biological tissues opaque, impeding deep tissue high-resolution optical imaging, manipulation, and therapy from reaching depths beyond approximately 1 mm, the transport mean free path[1]. In optical microscopy, many researchers explore the use of adaptive optics and wavefront shaping techniques to correct sample-induced aberrations, which can significantly enhance the sharpness of the point-spread function (PSF)[2–4]. These methods can be implemented physically by placing wavefront modulators in the excitation and detection paths[5–10], or computationally through wavefront correction algorithms. Some of the most advanced approaches can correct strong aberrations by estimating the aberration wavefront from multiple optical measurements, such as reflection matrix acquisition[11–17] or PSF scanning[5–8]. They have been successfully applied in modalities including optical coherence microscopy[11–17], second harmonic generation microscopy[18], fluorescence[9,10,19,20], and multiphoton microscopy[5,6,8,21]. Although these techniques do not require a physical guide star, their effectiveness typically depends on certain spatial invariance properties[9,10,19,20,22–26]. In particular, they often rely on local shift invariance when the PSF is spatially confined, but when the PSF becomes more extended, approximate shift invariance across a larger field of view is required for some of these techniques to remain effective. In the diffusive regime, typically at depths greater than 1 mm, these conditions are much more challenging to satisfy. The PSF becomes significantly broadened, and the isoplanatic patch size is markedly reduced. Both factors present substantial challenges for effective aberration correction in deep-tissue imaging. Nevertheless, from a physics point of view, light can be focused far beyond this diffusion limit in scattering media if the wavefront of the incident beam is optimized to achieve constructive interference at the focal point[27–30]. Guide star-assisted time-reversal is an efficient way of obtaining such a wavefront. In a time-reversal experiment, the outward propagating wavefront originating from a

Caltech Optical Imaging Laboratory, Andrew and Peggy Cherng Department of Medical Engineering, Department of Electrical Engineering, California Institute of Technology, Pasadena, CA, USA. e-mail: LVW@caltech.edu

guide star embedded in the medium is holographically recorded and phase conjugated, which will result in a time-reversed propagation of light tracing back to the guide star along the scrambled scattering routes[31–33].

Introducing such a guide star noninvasively is challenging. Therefore, researchers have developed virtual guide star mechanisms: guide stars do not emit light themselves but perturb or modulate diffused light that interacts with them. Various guide star mechanisms have been explored, including focused ultrasound[34–41], magnetic particles[42], photo-switchable molecules[43], and microbubbles[44]. However, two major gaps remain unaddressed. First, guide stars should ideally be point-like. When the guide star occupies a large region, not only is the resolution low, but also the focus intensity peak-to-background ratio (PBR) is low, which is inversely proportional to the number of speckle grains within the guide star region[35,43,45,46]. In practical applications, it is difficult to place point-like guide stars into tissue as desired. Agents introduced endogenously or exogenously to the tissue are likely to dissolve or disperse, occupying a region larger than the optical resolution, while focused ultrasound guide stars are also much larger than the optical resolution. Second, except for ultrasound modulation, it is hard to control the position of the guide star and thus the position of the focus for most proposed guide star mechanisms. Furthermore, focusing to a fixed point is insufficient for imaging, which requires steering the focus and interrogating an array of points. The memory effect can be used to steer the focus[19,32,47–49], moving it within the isoplanatic patch by tilting or shifting the wavefront. However, the size of this patch shrinks steeply with increasing depth to a micrometer scale within a depth of 1 mm[46], undermining the practicality.

Here, we propose a mechanism called iterative time-reversal guided by absorption nonlinearity (iTRAN) that can address both problems. First, we demonstrate that although the guide star agent occupies an extended layer rather than a concentrated point, through multiple iterations, the speckle pattern in the scattering medium can automatically converge to a single spot in a winner-takes-all manner thanks to a positive feedback loop that favors higher-intensity speckle grains. Second, we show that it is possible to shift the focus gradually out of the isoplanatic patch by applying one additional iTRAN iteration every time the focal point is shifted.

Results

Principle

Locally induced changes in optical properties can act as virtual guide stars within the perturbed region in a scattering medium. By illuminating the sample twice and subtracting the scattered optical fields exiting the tissue $\mathbf{E}_{\mathbf{out}}$ recorded before and after the perturbation, we can create a virtual field emitted from the guide star location[50,51]. In our proposed mechanism, this change in optical property is caused not by factors like particle motion or ultrasound pressure, but by the diffused incident light itself. The key concept of our technique is to generate the perturbation guide star iteratively, i.e., using time-reversed light to induce the perturbation in subsequent iterations.

Light-induced optical property changes are prevalent. In this work, we show that a possible option is the absorption nonlinearity induced by ground-state depletion. For a three-level molecule, its absorption coefficient μ_a decreases with illumination intensity I or the corresponding field amplitude $|E|$[52]:

$$\mu_a(|E|) = \frac{\mu_{a0}}{1+\frac{I}{I_s}} = \frac{\mu_{a0}}{1+\frac{|E|^2}{E_s^2}} \tag{1}$$

where μ_{a0} is the low intensity absorption coefficient and $I_s = \frac{h\nu}{\tau A}$ is the saturation intensity corresponding to a field strength E_s. Here A is the absorption cross section of the molecule, $h\nu$ is the photon energy and τ is the excited state lifetime. In our experiment, we use the eosin molecule, which has a long triplet state lifetime, leading to a low saturation intensity of 0.6 W cm^{-2} [53].

Iterations are carried out as follows. In the current iteration, an incoming field $\mathbf{E}_{\mathbf{in}}$ is incident on the surface of the scattering medium, whose wavefront can be modulated by a spatial light modulator (SLM). We detect the outgoing field $\mathbf{E}_{\mathbf{out}}$ from the same surface area, which is measured via digital holography. $\mathbf{E}_{\mathbf{out}}$ contains two components. The first component $R\boldsymbol{E}_{\mathbf{in}}$ does not interact with the nonlinear absorbers (i.e., the target eosin layer), where R is the reflection matrix depicting this linear process. A portion of the light arrives at the nonlinear absorbers with the field being

$$\mathbf{E}_{\mathbf{t}} = T\mathbf{E}_{\mathbf{in}} \tag{2}$$

where T is the transmission matrix in the absence of eosin absorption. This portion of light is additionally attenuated by the eosin layer with an effective reflection coefficient $r(|E_t|) = r_s e^{-\frac{\mu_a(|E_t|)d}{2}}$, where r_s is the backscattering coefficient and d is the effective path length inside the layer. The r factor varies spatially depending on the local field amplitude $|E_t|$. Propagating back to the surface, the field is multiplied by T^T, due to reciprocity. Thus, the outgoing field is

$$\mathbf{E}_{\mathbf{I,out}} = T^T r(|E_t|)\mathbf{E}_{\mathbf{t}} + R\mathbf{E}_{\mathbf{in}}, \tag{3}$$

where subscript **I** stands for low-intensity illumination, which is the case for our first measurement. We also note that this formulation can be readily extended to the more practical case of three-dimensionally distributed absorbing molecules and backscatterers. In this setting, T can be interpreted as a deposition matrix that relates the input field to the regional field distribution throughout the 3D volume[54,55]. This process is depicted in Fig. 1a. We then increase the amplitude of the incident field by a factor of γ and take the second measurement. As shown in Fig. 1b, a weaker grain and a stronger one (cap W and cap S) suffer from different extents of ground-state depletion. If the scattering medium is static between the measurements, the recorded field under high-intensity illumination can be expressed as

$$\mathbf{E}_{\mathbf{h,out}} = T^T r(\gamma|E_t|)\gamma\mathbf{E}_{\mathbf{t}} + \gamma R\mathbf{E}_{\mathbf{in}}. \tag{4}$$

We then subtract the two recorded fields with scaling as follows:

$$\mathbf{E}_{\mathbf{h,out}} - \gamma\mathbf{E}_{\mathbf{I,out}} = T^T\left[r(\gamma|E_t|) - r(|E_t|)\right]\gamma\mathbf{E}_{\mathbf{t}}. \tag{5}$$

As illustrated by Fig. 1c, with this calculation, the portion of light $\gamma R\mathbf{E}_{\mathbf{in}}$, which does not interact with the nonlinear absorber, is canceled. We have created a virtual source field that emits from the target layer, modulated by the difference in absorption by the nonlinear layer, denoted as $\Delta r(|E_t|) = r(\gamma|E_t|) - r(|E_t|)$. In the next iteration, as shown in Fig. 1 d, this digitally synthesized subtraction field is conjugated and projected through the SLM as the new input field:

$$\mathbf{E}_{\mathbf{in}}^{(i+1)} \propto \left(\mathbf{E}_{\mathbf{h,out}}^{(i)} - \gamma\mathbf{E}_{\mathbf{I,out}}^{(i)}\right)^*. \tag{6}$$

In this new iteration, the field reaching the eosin layer becomes

$$\mathbf{E}_{\mathbf{t}}^{(i+1)} \propto TT^\dagger \Delta r\left(\left|E_t^{(i)}\right|\right)\mathbf{E}_{\mathbf{t}}^{(i)*} \approx \Delta r\left(\left|E_t^{(i)}\right|\right)\mathbf{E}_{\mathbf{t}}^{(i)*}. \tag{7}$$

The operator $TT^\dagger$ is identity for a perfect time reversal, which holds approximately here. As shown in Fig. 1e and f, assuming perfect reproducibility of the field, we assert that through many iterations, $\mathbf{E}_{\mathbf{t}}$ will converge to a single speckle grain as can be seen by analyzing the weaker and stronger speckle grains of interest, W and S. In the i-th

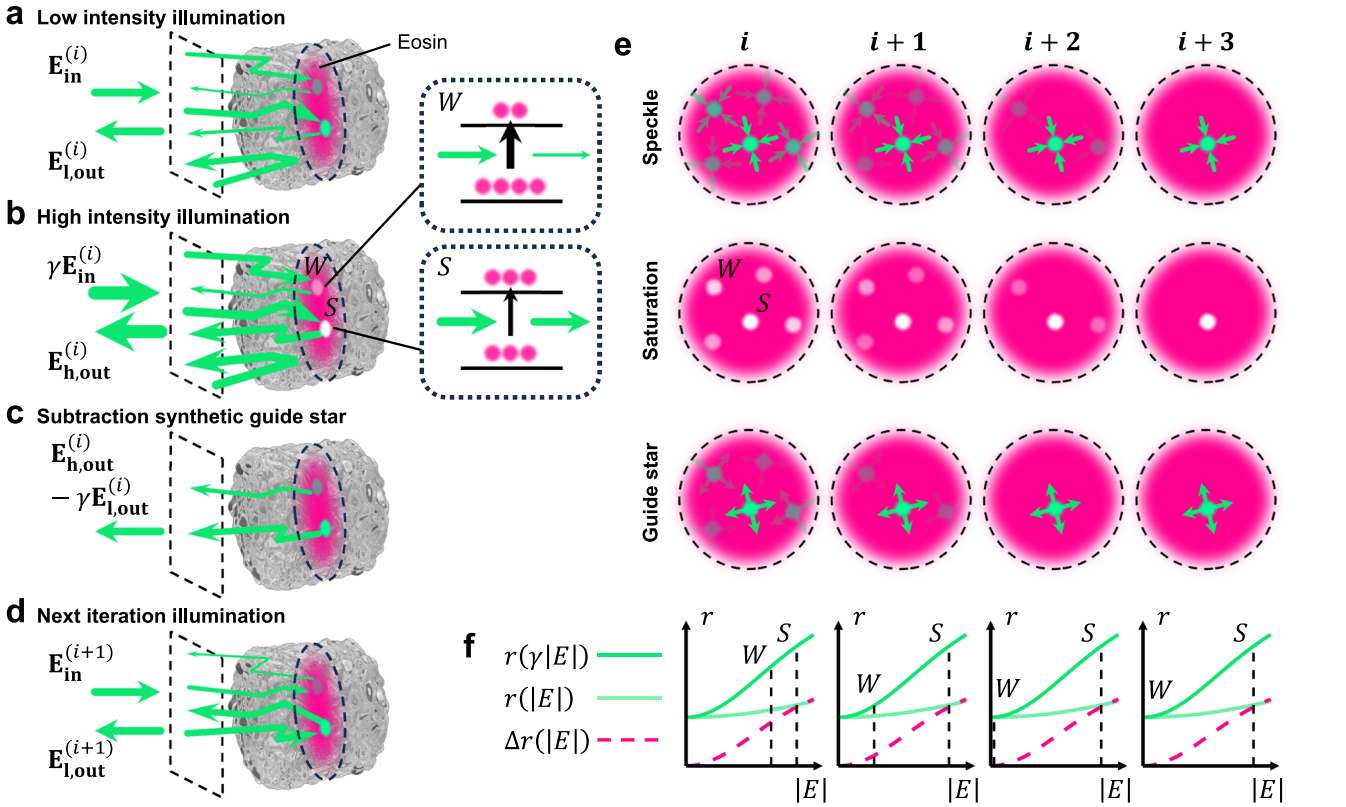

Fig. 1 | Principle of iTRAN. a, **b** Taking measurements under low and high-intensity illuminations. *S* (strong) and *W* (weak) represent the two speckle grains mentioned in the text. The insets illustrate the saturation mechanism via ground-state depletion for *S* and *W*. **c** Synthesizing virtual guide stars by scaled subtraction. **d** Taking measurement in the next iteration while time reversing the field emitted from the synthetic guide stars. In panel a-d, the low- and high-intensity incident fields ($\mathbf{E_{in}}$ and $\gamma\mathbf{E_{in}}$) and the corresponding outgoing measurement fields ($\mathbf{E_{l,out}}$ and $\mathbf{E_{h,out}}$) are defined on the same plane, indicated by the dashed boxes. Dashed circles indicate the target layer containing eosin within the scattering medium. Superscripts *i* and *i*+1 denote the iteration number. **e** Visualization of the winner-takes-all focusing mechanism. The three rows show (from top to bottom) the speckle pattern on the target layer, the eosin saturation level, and the resulting synthetic guide stars. Columns represent different iterations, as labeled at the top. The brightness of the dots and arrows reflects changes in speckle intensity, eosin saturation, and guide star strength over iterations. **f** Analyzing the convergence to a single speckle grain (i.e., a single guide star) via the effective reflection coefficient *r* and Δr mentioned in the text.

iteration, we have $\left|E_t^{(i)}(W)\right| < \left|E_t^{(i)}(S)\right|$. For the next iteration, we obtain

$$\frac{\left|E_t^{(i+1)}(W)\right|}{\left|E_t^{(i+1)}(S)\right|} = \frac{\Delta r\left(\left|E_t^{(i)}(W)\right|\right)}{\Delta r\left(\left|E_t^{(i)}(S)\right|\right)} \cdot \frac{\left|E_t^{(i)}(W)\right|}{\left|E_t^{(i)}(S)\right|}. \tag{8}$$

If in each iteration,

$$\frac{\Delta r\left(\left|E_t^{(i)}(W)\right|\right)}{\Delta r\left(\left|E_t^{(i)}(S)\right|\right)} < \frac{\left|E_t^{(i)}(W)\right|}{\left|E_t^{(i)}(S)\right|} \tag{9}$$

is satisfied, then $\frac{\left|E_t^{(i)}(W)\right|}{\left|E_t^{(i)}(S)\right|}$ will decay super-exponentially, by repeatedly multiplying a number smaller than itself. In other words, the weaker field becomes even weaker in each iteration. If this is valid for any pair of speckle grains, in the end only the strongest grain survives while all the others vanish. A key advantage of this process is that, ideally, the decay of the intensity ratio is not affected by the presence of other speckles, as the positive feedback occurs simultaneously across all speckle grains. This makes the approach particularly advantageous when the guide star region contains a large number of speckle modes, since convergence can still be achieved within a small number of iterations. This observation is further supported by the simulation results presented in Supplementary Section 6. Maintaining (9) requires proper adjustment of the incident power throughout the iterations (see supplementary section 4 for more information). Figure 1e illustrates the winner-take-all process, where the brightest speckle grain ultimately dominates, causing the other grains to dim in comparison. In real experiments, $TT^{\dagger}$ is not perfectly identity, and the speckles cannot be perfectly reproduced. Nonetheless, we have experimentally demonstrated that convergence can be achieved. A simulation was also conducted to study the impact of non-ideal time reversal arising from the limited number of control degrees of freedom (i.e., the column number of *T*) and the increasing number of speckle grains (i.e., the row number of *T*). See supplementary section 6 for details.

Focusing with iTRAN

Figure 2 shows the experimental realization of the scheme. As depicted in Fig. 2a, we use a 4 f system consisting of a lens and an objective to relay the SLM plane (SP) onto the surface of the scattering medium, where we can send the input field constructed in each iteration. The same 4 f system maps the outgoing field to the camera plane (CP), where it interferes with the reference beam for 4-step holographic measurement (see methods section and supplementary section 1 for more information). Figure 2a also illustrates using representative experimental data the scaled subtraction of the high- and low-intensity measurements and the construction of the next iteration's input field. Ideally, SP and CP are symmetric with respect to the beam splitter BS2, so that the two planes coincide after the 4 f system. However, because perfect alignment is difficult to achieve, we calibrate the system and

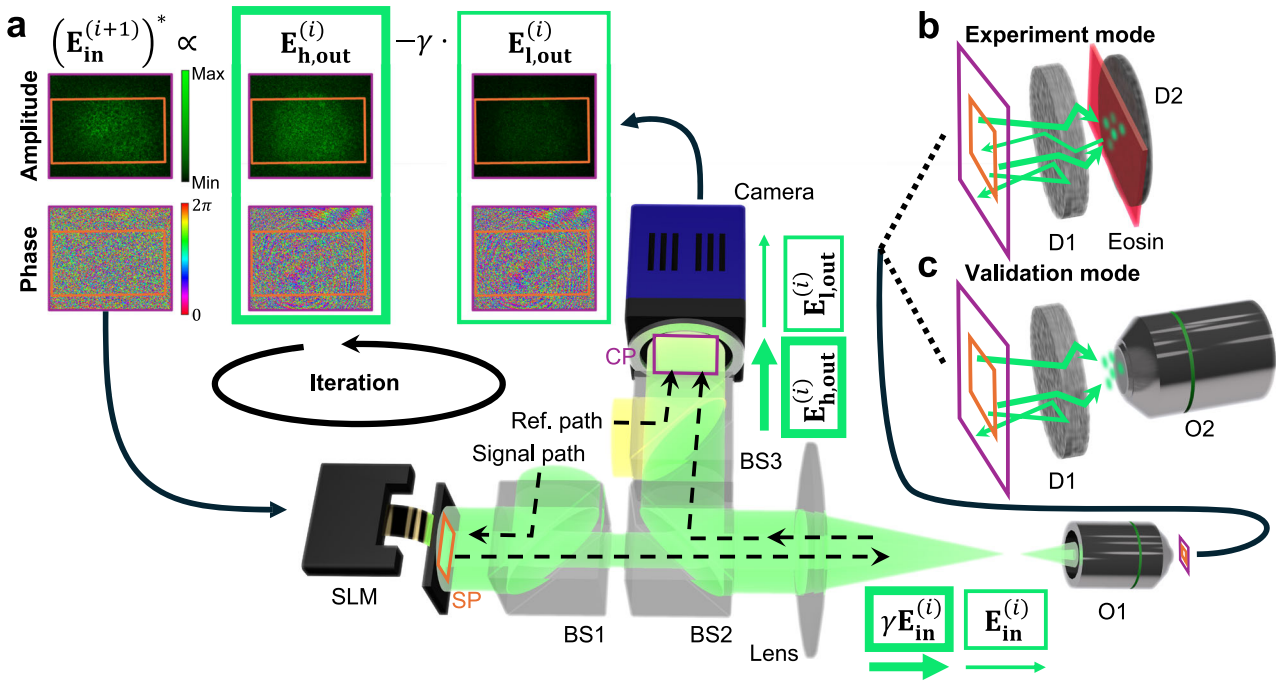

Fig. 2 | Experimental realization of iTRAN. a Experimental setup and signal flow. In the i-th iteration, low- and high-intensity fields $\mathbf{E}_{\mathbf{in}}^{(i+1)}$ and $\gamma\mathbf{E}_{\mathbf{in}}^{(i+1)}$ are relayed to the scattering medium via a 4 f system successively. Correspondingly, $\mathbf{E}_{\mathbf{l,out}}^{(i)}$ and $\mathbf{E}_{\mathbf{h,out}}^{(i)}$ are measured by the camera. Then adaptive subtraction is carried out (upper left), and the computed phase is displayed on the spatial light modulator (SLM) for the illumination in the next iteration. O1–2, optical objectives. BS1–3, non-polarizing beam splitters. SP SLM plane, CP camera plane. Dashed lines with arrows represent the optical paths followed by the signal and reference beams. **b**, **c** Continuation of the optical paths after O1 in (**a**). In experiment mode (b), the incident field is sent from the SLM, and the outgoing field is received by the camera. D1, diffuser with a tape attached to the back side; D2, reflective diffuser. In validation mode (**c**), D2 and the eosin layer are removed, and the computer-stored wavefronts in all iterations are played back sequentially. The resulting speckle pattern after D1 is relayed through O2 to another camera (not shown).

perform digital corrections (see supplementary section 3 for more information).

To imitate focusing into a scattering medium with the guide-star agent distributed inside, as shown in Fig. 2b, we sandwich an extended film made of eosin and gelatin (see methods for more information) between a transmission-based diffuser D1 (10 degrees Holographic Diffuser, Edmund Optics) and a reflective diffuser D2 (10 degrees, Thorlabs). To introduce more scattering and reduce the isoplanatic patch size, we attach a layer of Scotch tape to the back side of D1. In the first iteration, we display a spherical wavefront that can focus at a point on the eosin layer without the scattering medium, as shown in Fig. 3a. When the diffuser is in place, it becomes a broad distribution of speckles, as presented in both Fig. 3a and b. This result demonstrates that we are effectively mimicking the diffusive regime where no ballistic light component is present. Otherwise, a bright central spot would be observed. In each iteration, we record the wavefront displayed on the SLM in the computer's memory for later playback. After the last iteration, as shown in Fig. 2c, we remove the eosin layer along with the following diffuser and play back the stored wavefronts sequentially on the SLM. The transmitted field intensity is captured by another 4 f system relay and camera, allowing us to observe how the speckle pattern inside the scattering medium between D1 and D2 changes with iteration.

As seen in Fig. 3a, we observe the process of convergence to a single speckle grain. The focal point speckle grain becomes progressively stronger compared to other speckle grains throughout the iterations. Figure 3b shows another example in which we move the beam to another region on D1 to create another realization of the scattering medium. It should be noted that the focal point position is stochastic, i.e., it is likely to be different in different realizations of the scattering medium. Figure 3 d and 3e show the process of convergence via two metrics: the peak intensity calculated by the mean intensity of the pixels above 50% of the maximum value, and the area of the speckle pattern obtained by counting the number of pixels above 30% of the maximum value. The trends of both metrics are evident in the sequence of images shown in Supplementary Movies 1 and 2, corresponding to Fig.3a and b respectively. In Supplementary Movie 2, it is interesting to note that sometimes the weaker speckle grains can win against the stronger ones through iterations; during this process, the increase of peak intensity can be affected. This phenomenon can be caused by insufficient intensity scheduling (see supplementary section 4 for details), non-ideal time-reversal and photobleaching. The non-ideal time-reversal means a non-ideal reproducibility of the speckle pattern, i.e., the approximation of Eq. (7) has errors. If the error happens to weaken the stronger speckle grain and favor a weaker one, it can reverse the outcome of the competition. The photobleaching of eosin can also have a similar effect. If a strong speckle grain bleaches eosin, weakening the nonlinear absorption, then its Δr can be smaller, leading to a dimmer spot in the next iteration.

Steering focus beyond isoplanatic patch with iTRAN deaberration

Once an optical focus is formed, we can shift it by tilting the wavefront, i.e., adding a linear ramp to the phase pattern on the SLM. Without any additional steps, the process of progressively steering the focus is illustrated as $S_0, S_1, S_2,$ in Fig. 4a. When the steering distance increases, the focus becomes aberrated as the focus intensity decreases, and the background speckle intensity becomes more comparable to the focus intensity. Continuing to move the focus eventually obliterates the focus as the memory effect breaks down. To combat this problem, we propose doing one iteration of iTRAN after each steering step. If the shifting step size is not too large to the extent that the focus vanishes completely, the current focus remains the strongest speckle grain. By favoring the stronger grain and suppressing the weaker ones, iTRAN

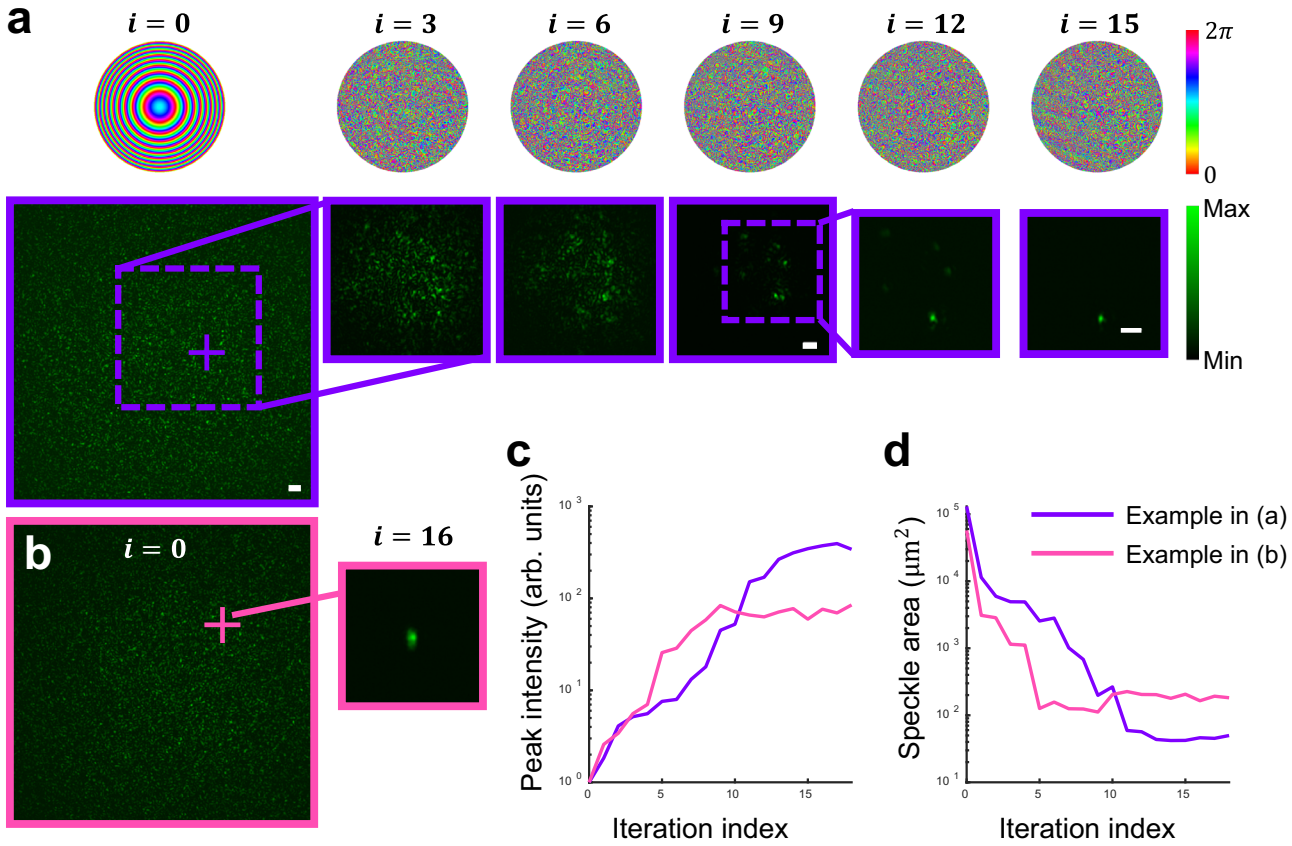

Fig. 3 | iTRAN focusing results. a Phase patterns on the SLM in the indicated iterations (upper row) and resulting speckle patterns behind the diffuser and tape (lower row). Scale bars: 20 μm. The cross on the initial speckle indicates the position where the focus converges. **b** iTRAN focusing through another region on D1, where the focus converges to a different location. **c**, **d** Peak intensity and speckle area versus the iteration index for (**a**) and (**b**), demonstrating the robustness of iTRAN.

de-aberrates the focus before the next steering step, resulting in $F1, F2, \cdots$ in Fig. 4a. Cumulatively, the focus can eventually be shifted out of the range of the isoplanatic patch. Figure 4b shows the experimental realization of the technique. Without de-aberration, the focus gradually becomes corrupted as we move to the 24th step. This behavior indicates that the combination of the diffuser and tape does not mimic a thin scattering medium, which aligns with our goal of operating in the diffusive regime, as evidenced by the very weak tilt-tilt memory effect. With de-aberration, the focus can be maintained as it shifts downward (see Supplementary Movie 3 for all the steps). It is also observed that the focus resolution and quality degrade during the scanning process. This is likely due to signal-to-noise ratio (SNR) degradation in the recorded hologram, which is exacerbated by the intensity scheduling applied in iTRAN, as well as from imperfect time reversal. Components near the edge of the aperture are more susceptible to the SNR decrease, effectively reducing the achievable numerical aperture and thereby degrading the resolution.

Discussion

One inherent limitation of the iTRAN focusing process is the uncertainty of where the focus initially converges. The steering strategy introduced in this work offers a way to control the relative position between the initial focus and subsequent ones. To allow the focus to be freely repositioned across the entire field of view, the steering process must remain stable over numerous isoplanatic patches, rather than being limited to just a few. In theory, iTRAN offers a key advantage: the virtual guide star, created by the nonlinearity-induced perturbation, moves along with the focus. Once the focus is shifted from point A to point B through a sequence of steering and iTRAN operations, the virtual guide star is effectively relocated to B, and the center of the isoplanatic patch is redefined at B rather than A. Subsequent steering from B proceeds independently of the original isoplanatic patch around A. However, in practice, several factors may cause the focus to vanish or shift to an unintended location that deviates from the designed scanning path, especially as the scan progresses over a larger field of view. These include insufficient SNR, additional aberrations introduced by non-ideal time reversal, and photobleaching of the nonlinear absorber. In Fig. 4, we present a successful scan consisting of 45 consecutive steps, which represents a typical achievable length with our current system. The stability of the process can be improved by increasing the operation speed, thereby reducing field subtraction errors caused by system instability, and by decreasing the scanning step size to ease the burden on the de-aberration. Nonetheless, we anticipate that arbitrarily controllable focus may be achieved by initially placing the focus near the surface, where aberrations are minimal, and then steering it progressively into deeper regions. Because the memory effect also exists in the axial direction[56–58], it is possible to apply a similar iTRAN-based de-aberration strategy to drill the focus deeper. A proof-of-concept experiment demonstrating this approach is shown in Fig. S8 in Supplementary Section 5.

In this work, iTRAN is demonstrated only for a single two-dimensional layer of nonlinear absorbers, which raises concerns about its applicability to more realistic scenarios involving three-dimensionally distributed nonlinear agents within volumetric scattering media. Extending the technique to such 3D cases will be a key direction of our future research. In supplementary section 5, we discuss potential direct applications of the current method, along with strategies for advancing it toward extension to fully 3D scenarios. We

https://doi.org/10.1038/s41467-025-63095-w

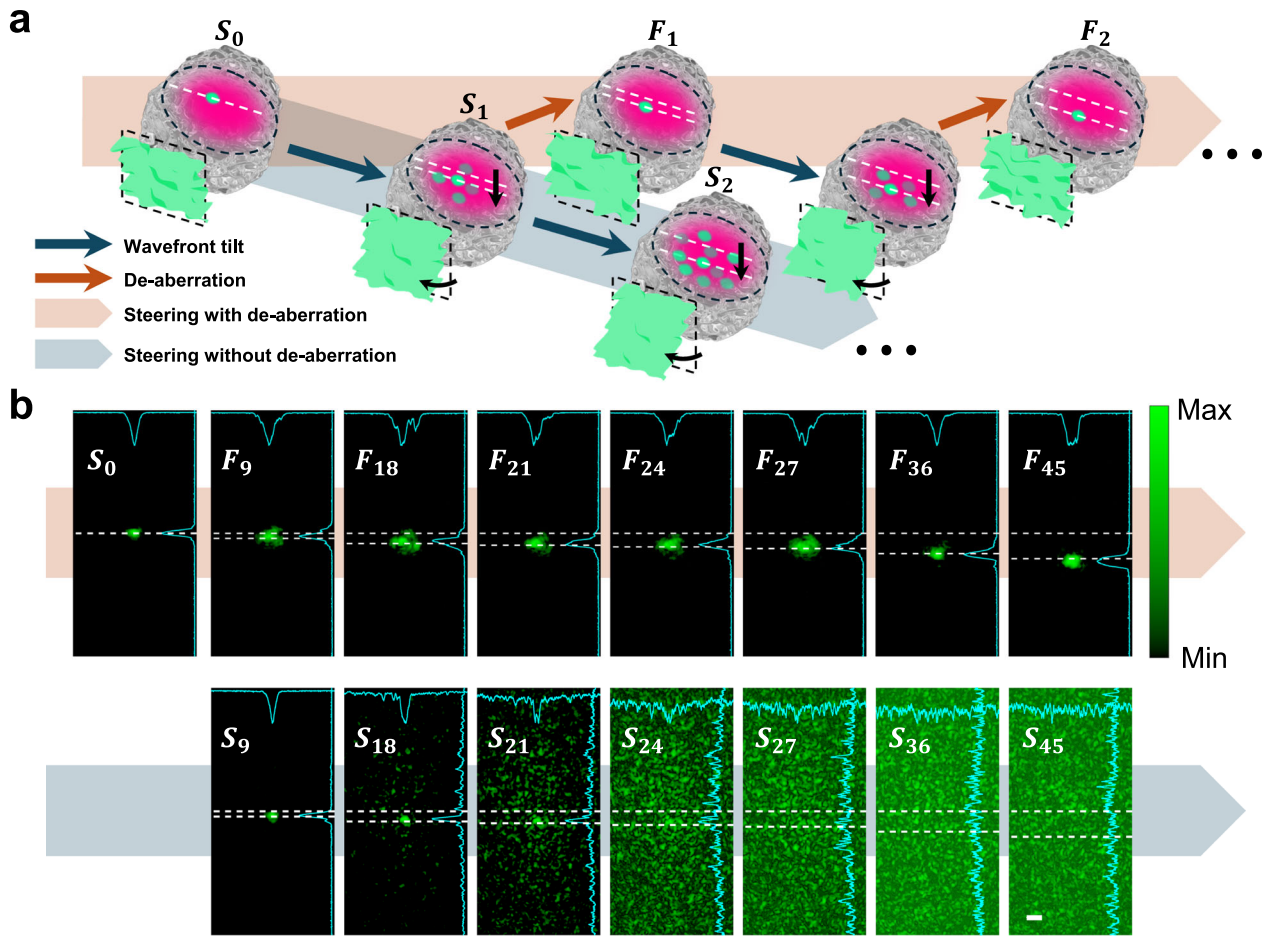

Fig. 4 | iTRAN steering of the focus with de-aberration beyond the isoplanatic patch. a Visualization of steering the focus with and without iTRAN de-aberration. Without de-aberration, we run through internal speckles S_0, S_1 and S_2. Wavefront tilting (black curved arrow) shifts downward the focus, as shown by the internal speckles S_0, S_1, S_2, but along with increasing aberration. With de-aberration by taking one iTRAN iteration after each focal shift, the focus can be maintained as shown in the internal speckles F_1 and F_2. **b** Experimental realization of steering the focus with (first row) and without de-aberration (second row). Scale bar, 20 μm. The line profiles represent the maximum intensity projections along the horizontal and vertical directions. White dashed lines align the starting position and the shifted positions of each focus.

also present preliminary data using a double-layer eosin configuration and a volumetric phantom composed of eosin powder dispersed in epoxy.

Another limitation of the current experiments is that the eosin layer is uniform, which represents an overly idealized scenario compared to realistic applications, where the concentration of the nonlinear absorbers is typically nonuniform. In the extreme case where a region contains a persistently low concentration of absorbers, the iTRAN focus has little to no chance of converging there. During focus steering, entering such a region may lead to the disappearance of the focus. However, as shown in supplementary section 8, when the nonuniformity is not severe, iTRAN can still achieve focus and successfully steer through the nonuniform region. Thus, for imaging applications, it is important to ensure that the guide star molecules are present at sufficient concentration throughout the region of interest, while also avoiding highly heterogeneous distributions that could disrupt the focus steering. Whereas in applications such as optogenetics or light-based therapy, such spatial specificity is often desirable and can be achieved through techniques such as genetic targeting[59], receptor-mediated delivery[60,61], or accumulation in tumors via the enhanced permeability and retention effect[62].

Although time reversal does not impose a fundamental physical limit on the optical thickness for light focusing, the performance of this method at increasing depths is ultimately constrained by SNR degradation, similar to other guide-star-assisted time reversal techniques. As the imaging depth increases, fewer photons reach the target region and interact with the guide star molecules to generate the virtual guide star signal. Large fraction of photons are backscattered or absorbed within the medium before reaching the intended depth. However, two features of our approach help mitigate this limitation. First, as the iTRAN iterations progress, the intensity at the guide star region increases steeply, which enhances the SNR by improving the efficiency of the nonlinear perturbation. Second, in the steering-plus-iteration scheme, the nonlinear interaction occurs precisely at the focus location and not across a wide field, making the perturbation process significantly more efficient compared to schemes that rely on widefield illumination and isolated point-like guide stars.

Moving towards applications with real biological tissue, we may need a nonlinear agent that suffers less from photobleaching, which would lead to a more stable focus. Another drawback of the eosin molecule is that it suffers from oxygen quenching, which decreases the triplet state lifetime. If not dissolved in the gelatin film to isolate from oxygen, eosin does not exhibit the desired low saturation intensity. Although ground-state depletion saturable absorption is used in our study, in principle, the technique can be extended to other nonlinear mechanisms. Provided the medium is altered by the incident light, which in turn perturbs the light, our methodology can be applied. For instance, light-induced absorption change can also be achieved by

photo-switchable proteins. The nonlinearity does not need to exhibit a saturation curve; it can also be a nonlinearly increasing curve (see supplementary section 7 for a discussion of different nonlinear functional forms). Nor is it even limited to absorption. Other nonlinear effects, such as multiphoton absorption, second harmonic generation, and stimulated Raman scattering, also have a nonlinear response to incident light intensity. These effects can be more desirable for biological tissue because exogenous contrast chromophores are not needed.

The technique may be of much interest to photodynamic therapy, where inefficient light delivery into deep tissue is a notorious problem[63]. We have shown in Fig. 3c that the intensity increase in iTRAN is dramatic even in the first few iterations. Additionally, the guide star agent might also function as the photosensitizer at the same time. In fact, eosin is the first photosensitizer used in photodynamic therapy[64]. The long triplet state lifetime that gives rise to its low saturation intensity is also a common feature of photosensitizers, as they usually produce singlet oxygen through the triplet state[65].

In the end, we want to draw an analogy between our method and the mode-locking of lasers. In passive mode locking, an optical pulse circulates in the laser cavity, and saturable absorbers are used to suppress the lower intensity peaks while favoring higher intensity peaks, resulting in a single pulse of high intensity after multiple roundtrips[66]. Our experiment resembles this process in the spatial domain, whereas our iteration involves phase conjugation and subtraction, with the light passing through a scattering medium.

In conclusion, we have conceived and experimentally demonstrated that an absorption nonlinearity guide star combined with iterative time reversal can produce a self-converging focusing effect in scattering media. The guide star agent can be spatially extended rather than concentrated at a point, while the iterations lead to convergence to a speckle scale focus. Our approach does not require metric-based optimization algorithms, which usually take numerous iterations to form a focus[24,67–69]. Moreover, our method can be used to scan and deaberrate the focus beyond the isoplanatic patch.

Methods

Experimental setup

The experimental setup is shown in Supplementary Fig. S1. The output from a 532 nm wavelength laser (Verdi G, Coherent) is split into a signal path and a reference path, each passing through an acoustic optical modulator (AOM) (AF1, IntraAction). Both beams are spatially filtered by passing through single-mode fibers and then expanded. The wavefront of the signal beam is modulated by the spatial light modulator (PLUTO, HOLOEYE). The AOMs introduce a 10 Hz frequency difference between them, synchronized with the camera (PCO.edge 5.5, PCO) operating at a 40 Hz frame rate, allowing us to perform 4-step holography measurements. With additional beam splitters and photodiodes, we monitor the intensity of the input signal beam and reference beam. During the scaled subtraction, we correct for the amplitude scaling of the measured field due to adjustment of reference beam intensity and exposure time. We also compensate for the unwanted phase difference between the high- and low-intensity fields (see supplementary sections 1 and 2 for more information). We note that our current experimental setup is not optimized for high-speed operation due to limitations in hardware configuration, the time required for pixel-matching digital adjustments (see supplementary section 3), and delays associated with displaying intermediate results. As a result, one iteration currently takes approximately 14 seconds. However, techniques for achieving high-speed digital phase conjugation are readily available. The record for the lowest latency in digital phase conjugation is on the millisecond scale[70–72], and this has continued to improve[73]. In our case, the only additional computational step required is a simple scaled subtraction, which is inexpensive and can be easily implemented.

Eosin layer preparation

We prepare the eosin sample by mixing 2.5 mL of 0.1% eosin solution (Eosin Yellowish, Thermo Fisher Scientific) with 50 mL of 10% gelatin (Type B, Thermo Fisher Scientific). The mixture is heated to 50 °C and poured onto a flat surface, allowing surface tension to create a puddle. Once the puddle dries, it forms a thin layer.

Data availability

The experimental data generated in this study are provided in the Supplementary Information or available from the corresponding author upon request.

Code availability

The code implemented in this study is available from the authors upon request.

References

1. Wang, L. V. & Wu, H. *Biomedical Optics: Principles and Imaging*. (John Wiley & Sons, 2007).
2. Hampson, K. M. et al. Adaptive optics for high-resolution imaging. *Nat. Rev. Methods Prim.* **1**, 68 (2021).
3. Ji, N. Adaptive optical fluorescence microscopy. *Nat. Methods* **14**, 374–380 (2017).
4. Zhang, Q. et al. Adaptive optics for optical microscopy. *Biomed. Opt. Express* **14**, 1732–1756 (2023).
5. Papadopoulos, I. N., Jouhanneau, J.-S., Poulet, J. F. & Judkewitz, B. Scattering compensation by focus scanning holographic aberration probing (F-SHARP). *Nat. Photonics* **11**, 116–123 (2017).
6. Papadopoulos, I. N. et al. Dynamic conjugate F-SHARP microscopy. *Light Sci. Appl.* **9**, 110 (2020).
7. May, M. A. et al. Fast holographic scattering compensation for deep tissue biological imaging. *Nat. Commun.* **12**, 4340 (2021).
8. Qin, Z. et al. Deep tissue multi-photon imaging using adaptive optics with direct focus sensing and shaping. *Nat. Biotechnol.* **40**, 1663–1671 (2022).
9. Aizik, D., Gkioulekas, I. & Levin, A. Fluorescent wavefront shaping using incoherent iterative phase conjugation. *Optica* **9**, 746–754 (2022).
10. Aizik, D. & Levin, A. Non-invasive and noise-robust light focusing using confocal wavefront shaping. *Nat. Commun.* **15**, 5575 (2024).
11. Yoon, S., Lee, H., Hong, J. H., Lim, Y.-S. & Choi, W. Laser scanning reflection-matrix microscopy for aberration-free imaging through intact mouse skull. *Nat. Commun.* **11**, 5721 (2020).
12. Kwon, Y. et al. Computational conjugate adaptive optics microscopy for longitudinal through-skull imaging of cortical myelin. *Nat. Commun.* **14**, 105 (2023).
13. Kang, S. et al. Tracing multiple scattering trajectories for deep optical imaging in scattering media. *Nat. Commun.* **14**, 6871 (2023).
14. Lee, Y.-R., Kim, D.-Y., Jo, Y., Kim, M. & Choi, W. Exploiting volumetric wave correlation for enhanced depth imaging in scattering medium. *Nat. Commun.* **14**, 1878 (2023).
15. Badon, A. et al. Smart optical coherence tomography for ultra-deep imaging through highly scattering media. *Sci. Adv.* **2**, e1600370 (2016).
16. Badon, A. et al. Distortion matrix concept for deep optical imaging in scattering media. *Sci. Adv.* **6**, eaay7170 (2020).
17. Balondrade, P. et al. Multi-spectral reflection matrix for ultrafast 3D label-free microscopy. *Nat. Photonics* **18**, 1097–1104 (2024).
18. Murray, G. et al. Aberration free synthetic aperture second harmonic generation holography. *Opt. Express* **31**, 32434–32457 (2023).
19. Boniface, A., Dong, J. & Gigan, S. Non-invasive focusing and imaging in scattering media with a fluorescence-based transmission matrix. *Nat. Commun.* **11**, 6154 (2020).

20. Zhu, L. et al. Large field-of-view non-invasive imaging through scattering layers using fluctuating random illumination. *Nat. Commun.* **13**, 1447 (2022).
21. Tang, J., Germain, R. N. & Cui, M. Superpenetration optical microscopy by iterative multiphoton adaptive compensation technique. *Proc. Natl. Acad. Sci.* **109**, 8434–8439 (2012).
22. Bertolotti, J. et al. Non-invasive imaging through opaque scattering layers. *Nature* **491**, 232–234 (2012).
23. Katz, O., Small, E. & Silberberg, Y. Looking around corners and through thin turbid layers in real time with scattered incoherent light. *Nat. Photonics* **6**, 549–553 (2012).
24. Yeminy, T. & Katz, O. Guidestar-free image-guided wavefront shaping. *Sci. Adv.* **7**, eabf5364 (2021).
25. Feng, B. Y. et al. NeuWS: Neural wavefront shaping for guidestar-free imaging through static and dynamic scattering media. *Sci. Adv.* **9**, eadg4671 (2023).
26. Haim, O., Boger-Lombard, J. & Katz, O. Image-guided computational holographic wavefront shaping. *Nat. Photonics* **19**, 44–53 (2025).
27. Shen, Y., Liu, Y., Ma, C. & Wang, L. V. Focusing light through biological tissue and tissue-mimicking phantoms up to 9.6 cm in thickness with digital optical phase conjugation. *J. Biomed. Opt.* **21**, 085001–085001 (2016).
28. Vellekoop, I. M. & Mosk, A. P. Focusing coherent light through opaque strongly scattering media. *Opt. Lett.* **32**, 2309–2311 (2007).
29. Vellekoop, I. M. Feedback-based wavefront shaping. *Opt. Express* **23**, 12189–12206 (2015).
30. Cheng, Z., Li, C., Khadria, A., Zhang, Y. & Wang, L. V. High-gain and high-speed wavefront shaping through scattering media. *Nat. Photonics* **17**, 299–305 (2023).
31. Horstmeyer, R., Ruan, H. & Yang, C. Guidestar-assisted wavefront-shaping methods for focusing light into biological tissue. *Nat. Photonics* **9**, 563–571 (2015).
32. Yaqoob, Z., Psaltis, D., Feld, M. S. & Yang, C. Optical phase conjugation for turbidity suppression in biological samples. *Nat. Photonics* **2**, 110–115 (2008).
33. Vellekoop, I. M. & Mosk, A. P. Universal Optimal Transmission of Light Through Disordered Materials. *Phys. Rev. Lett.* **101**, 120601 (2008).
34. Xu, X., Liu, H. & Wang, L. V. Time-reversed ultrasonically encoded optical focusing into scattering media. *Nat. Photonics* **5**, 154–157 (2011).
35. Wang, Y. M., Judkewitz, B., DiMarzio, C. A. & Yang, C. Deep-tissue focal fluorescence imaging with digitally time-reversed ultrasound-encoded light. *Nat. Commun.* **3**, 928 (2012).
36. Si, K., Fiolka, R. & Cui, M. Breaking the spatial resolution barrier via iterative sound-light interaction in deep tissue microscopy. *Sci. Rep.* **2**, 748 (2012).
37. Judkewitz, B., Wang, Y. M., Horstmeyer, R., Mathy, A. & Yang, C. Speckle-scale focusing in the diffusive regime with time reversal of variance-encoded light (TROVE). *Nat. Photonics* **7**, 300–305 (2013).
38. Cheng, Z. & Wang, L. V. Focusing light into scattering media with ultrasound-induced field perturbation. *Light Sci. Appl.* **10**, 159 (2021).
39. Ma, C., Xu, X. & Wang, L. V. Analog time-reversed ultrasonically encoded light focusing inside scattering media with a 33,000\times optical power gain. *Sci. Rep.* **5**, 8896 (2015).
40. Liu, Y. et al. Time-reversed ultrasonically encoded optical focusing through highly scattering ex vivo human cataractous lenses. *J. Biomed. Opt.* **23**, 010501–010501 (2018).
41. Suzuki, Y., Tay, J. W., Yang, Q. & Wang, L. V. Continuous scanning of a time-reversed ultrasonically encoded optical focus by reflection-mode digital phase conjugation. *Opt. Lett.* **39**, 3441–3444 (2014).
42. Ruan, H. et al. Focusing light inside scattering media with magnetic-particle-guided wavefront shaping. *Optica* **4**, 1337–1343 (2017).
43. Yang, J. et al. Focusing light inside live tissue using reversibly switchable bacterial phytochrome as a genetically encoded photochromic guide star. *Sci. Adv.* **5**, eaay1211 (2019).
44. Ruan, H., Jang, M. & Yang, C. Optical focusing inside scattering media with time-reversed ultrasound microbubble encoded light. *Nat. Commun.* **6**, 8968 (2015).
45. Vellekoop, I. M., Van Putten, E. G., Lagendijk, A. & Mosk, A. P. Demixing light paths inside disordered metamaterials. *Opt. Express* **16**, 67–80 (2008).
46. Judkewitz, B., Horstmeyer, R., Vellekoop, I. M., Papadopoulos, I. N. & Yang, C. Translation correlations in anisotropically scattering media. *Nat. Phys.* **11**, 684–689 (2015).
47. Freund, I., Rosenbluh, M. & Feng, S. Memory Effects in Propagation of Optical Waves through Disordered Media. *Phys. Rev. Lett.* **61**, 2328–2331 (1988).
48. Osnabrugge, G., Horstmeyer, R., Papadopoulos, I. N., Judkewitz, B. & Vellekoop, I. M. Generalized optical memory effect. *Optica* **4**, 886–892 (2017).
49. Kubby, J., Gigan, S. & Cui, M. *Wavefront Shaping for Biomedical Imaging*. (Cambridge University Press, 2019).
50. Ma, C., Xu, X., Liu, Y. & Wang, L. V. Time-reversed adapted-perturbation (TRAP) optical focusing onto dynamic objects inside scattering media. *Nat. Photonics* **8**, 931–936 (2014).
51. Zhou, E. H., Ruan, H., Yang, C. & Judkewitz, B. Focusing on moving targets through scattering samples. *Optica* **1**, 227–232 (2014).
52. Keyes, R. W. Nonlinear absorbers of light. *IBM J. Res. Dev.* **7**, 334–336 (1963).
53. Silberberg, Y. & Bar-Joseph, I. Transient effects in degenerate four-wave mixing in saturable absorbers. *IEEE J. Quantum Electron* **17**, 1967–1970 (1981).
54. Cao, H., Mosk, A. P. & Rotter, S. Shaping the propagation of light in complex media. *Nat. Phys.* **18**, 994–1007 (2022).
55. McIntosh, R. et al. Delivering broadband light deep inside diffusive media. *Nat. Photonics* **18**, 744–750 (2024).
56. Horisaki, R., Okamoto, Y. & Tanida, J. Single-shot noninvasive three-dimensional imaging through scattering media. *Opt. Lett.* **44**, 4032–4035 (2019).
57. Aarav, S. & Fleischer, J. W. Using speckle correlations for single-shot 3D imaging. *Appl. Opt.* **62**, D181–D186 (2023).
58. Aarav, S. & Fleischer, J. W. Depth-resolved speckle correlation imaging using the axial memory effect. *Opt. Express* **32**, 23750–23757 (2024).
59. Packer, A. M., Roska, B. & Häusser, M. Targeting neurons and photons for optogenetics. *Nat. Neurosci.* **16**, 805–815 (2013).
60. Sharman, W. M., van Lier, J. E. & Allen, C. M. Targeted photodynamic therapy via receptor mediated delivery systems. *Adv. Drug Deliv. Rev.* **56**, 53–76 (2004).
61. Wang, X. et al. The development of site-specific drug delivery nanocarriers based on receptor mediation. *J. Controlled Release* **193**, 139–153 (2014).
62. Iyer, A. K., Khaled, G., Fang, J. & Maeda, H. Exploiting the enhanced permeability and retention effect for tumor targeting. *Drug Discov. Today* **11**, 812–818 (2006).
63. Algorri, J. F., Ochoa, M., Roldan-Varona, P., Rodriguez-Cobo, L. & López-Higuera, J. M. Light technology for efficient and effective photodynamic therapy: a critical review. *Cancers* **13**, 3484 (2021).
64. Dolmans, D. E., Fukumura, D. & Jain, R. K. Photodynamic therapy for cancer. *Nat. Rev. Cancer* **3**, 380–387 (2003).
65. Takemura, T., Ohta, N., Nakajima, S. & Sakata, I. Critical importance of the triplet lifetime of photosensitizer in photodynamic therapy of tumor. *Photochem. Photobiol.* **50**, 339–344 (1989).
66. Ippen, E. P. Principles of passive mode locking. *Appl. Phys. B Laser Opt.* **58**, 159–170 (1994).
67. Woo, C. M. et al. Optimal efficiency of focusing diffused light through scattering media with iterative wavefront shaping. *APL Photonics* **7**, 046109 (2022).

68. Lai, P., Wang, L., Tay, J. W. & Wang, L. V. Photoacoustically guided wavefront shaping for enhanced optical focusing in scattering media. *Nat. Photonics* **9**, 126–132 (2015).
69. Tay, J. W., Lai, P., Suzuki, Y. & Wang, L. V. Ultrasonically encoded wavefront shaping for focusing into random media. *Sci. Rep.* **4**, 3918 (2014).
70. Wang, D. et al. Focusing through dynamic tissue with millisecond digital optical phase conjugation. *Optica* **2**, 728–735 (2015).
71. Liu, Y., Ma, C., Shen, Y., Shi, J. & Wang, L. V. Focusing light inside dynamic scattering media with millisecond digital optical phase conjugation. *Optica* **4**, 280–288 (2017).
72. Hemphill, A. S., Shen, Y., Liu, Y. & Wang, L. V. High-speed single-shot optical focusing through dynamic scattering media with full-phase wavefront shaping. *Appl. Phys. Lett.* **111**, 221109 (2017).
73. Luo, J. et al. High-speed single-exposure time-reversed ultrasonically encoded optical focusing against dynamic scattering. *Sci. Adv.* **8**, eadd9158 (2022).

Acknowledgements

The authors would like to thank Yan Liu, Yousuf Aborahama, Yide Zhang, Zhe He, and Geng Ku for their valuable discussions and assistance. This work was supported in part by National Institutes of Health grant R35 CA220436 (Outstanding Investigator Award to L.V.W.), and by grant number 2024-337784 from the Chan Zuckerberg Initiative DAF, an advised fund of the Silicon Valley Community Foundation, also awarded to L.V.W.

Author contributions

M.C. and L.V.W. initiated the project; M.C. and S.S.K. designed and ran the experiments. M.C. and S.S.K. wrote the code for the experiments and simulations. L.V.W. provided overall supervision. All authors were involved in writing the manuscript.

Competing interests

L.V.W. has a financial interest in Microphotoacoustics, Inc., CalPACT, LLC., and Union Photoacoustic Technologies, Ltd., which, however, did not support this work. The other authors declare no competing interests.

Additional information

Supplementary information The online version contains supplementary material available at https://doi.org/10.1038/s41467-025-63095-w.

Correspondence and requests for materials should be addressed to Lihong V. Wang.

Peer review information *Nature Communications* thanks Mooseok Jang and the other anonymous reviewer(s) for their contribution to the peer review of this work. A peer review file is available.